

Gate optimization for resin transfer molding in dual-scale porous media: Numerical simulation and experiment measurement

Yutaka Oya¹ , Tsubasa Matsumiya¹, Akira Ito¹,
Ryosuke Matsuzaki^{2,3}  and Tomonaga Okabe^{1,4}

Abstract

For resin transfer molding in a woven fabric, this study developed a novel framework for optimization by combining a multi-objective genetic algorithm and mold-filling simulation including a void-formation model, which gives us not only the spatial distribution of the mesoscopic and microscopic voids but also the correlations between molding characteristics such as fill time, total amount of void, weld line, and wasted resin. Our experiment observation of one-point radial injection successfully captured the anisotropic distribution of mesoscopic voids, which qualitatively validates the simulated result. As a result of multi-objective optimization for an arrangement of two injection positions, we found the trade-off relations of weld line with the other characteristics, which also have positive correlation with each other. Furthermore, visualization techniques such as self-organizing maps and parallel coordinate maps extracted the design rule of the arrangement. For example, a diagonal gate arrangement with an appropriate distance is required for reducing the both total amount of voids, fill time, and wasted resin; however, the total area of the weld line becomes relatively large. Our framework and the knowledge obtained from this study will enable us to determine the appropriate mold design for resin transfer molding.

Keywords

Finite element analysis, resin transfer molding, multi-objective optimization

Introduction

In the past few decades, fiber-reinforced plastic (FRP) has been widely used for structural parts in the aerospace and automobile fields, due to their high specific strength and stiffness.¹ Resin transfer molding (RTM) has become an attractive process for manufacturing a large number of FRPs because of its high efficiency and low cost compared to conventional autoclave molding. In RTM, low-viscosity resin is usually injected into preplaced reinforcement material where a random fiber mat and a woven fabric are commonly used as the reinforcement. Although a random mat is an isotropic media for fluid, woven fabric has a microscopic flow path inside the fiber bundle in addition to an inter-bundle region; thus, it is known as dual-scale porous medium.^{2–7} The velocity difference between the intra-bundle and inter-bundle paths causes air entrapment (void), which degrades the mechanical properties of the FRP.^{8,9} If the velocity of the

intra-bundle (inter-bundle) region exceeds that of the inter-bundle (intra-bundle) region, a void is generated in the inter-bundle (intra-bundle) region. A void formed in the inter-bundle region is known as a mesoscopic void, whereas air entrapment inside the fiber bundle^{10–13} is known as a microscopic void. It should be noted that a macroscopic void (also called a dry spot^{10,14}) is a dry region where the fabric is not

¹Department of Aerospace Engineering, Tohoku University, Japan

²Department of Mechanical Engineering, Tokyo University of Science, Japan

³Institute of Fluid Science, Tohoku University, Japan

⁴Department of Materials Science and Engineering, University of Washington, USA

Corresponding author:

Yutaka Oya, Tohoku University, 6-6-01 Aramaki-Aza-Aoba, Aoba-ku, Sendai, Miyagi 980-8579, Japan.

Email: oya@plum.mech.tohoku.ac.jp

impregnated by resin in either the inter- or intra-bundle regions. This velocity difference comes from a different dominant force in each flow path. Flow in the inter-bundle region is driven mainly by viscous force, whereas capillary force is dominant in the intra-bundle region. Therefore, the flow in each path should be considered independently.

Several researchers have investigated resin flow in the intra-bundle flow path.^{15–18} Foley et al.¹⁵ conducted a numerical simulation inside the fiber bundle and demonstrated that surface tension, contact angle, and fiber diameter strongly affect the rate of impregnation into the fiber bundle. These parameters are not usually considered in the macroscopic governing equation (Darcy's law). In an effort to reproduce advancement of resin in the intra-bundle region, Kang et al.¹¹ modified Darcy's law by considering the capillary effect. They developed a mathematical model based on the experiment result to analyze void formation. Their experiment result confirmed that the void content was related to the modified capillary number Ca^* , which is expressed as

$$Ca^* = \frac{\mu U}{\gamma \cos \theta} \quad (1)$$

where μ is resin viscosity, U is global resin velocity, γ is the surface tension of the resin, and θ is the contact angle between the resin and the fiber fabric. Garcia et al.¹⁹ simulated distribution of microscopic and mesoscopic voids by two phase flow models of air and resin. Park et al.¹² proposed the void formation model in consideration of woven fabric structure of reinforced mat. They evaluated void content based on the time difference in resin impregnation between the inter-bundle and intra-bundle regions and agreed well with experiment data. This model also enables us to evaluate void contents depending on tow orientations. Matsuzaki et al.²⁰ also conducted a unidirectional experiment to obtain the mesoscopic void contents of woven fabric on the basis of a different concept from Park et al.

In order to extract optimum molding conditions, it is important to predict distribution of microscopic and mesoscopic void depending on structure of woven fabric. For predicting the distribution of voids, flow-filling simulation combined with void formation model proposed by Park et al.¹² is an effective way. In this study, we combined this void-formation model with resin filling simulation based on finite element method (FEM). This study also conducted experiments of one-point radial injection to compare simulated distributions of mesoscopic voids. Furthermore, to obtain appropriate molding conditions establishing both productivity and quality, the framework of multi-objective optimization (MOO) is newly developed as the combination of this filling simulation and the gene algorithm (GA) to search global

optimum solutions (Pareto solutions) for multi-disciplinary characteristics.^{21–23} This study considers the two-dimensional square system and an arrangement of two-injection positions of resin as a design variable. For industrial application, the multi-injection location has been considered an efficient way to increase the productivity of RTM; however, conjunction of resin flows from different injection locations induces another defect known as weld line. Therefore, total voids (sum of mesoscopic and microscopic voids), filling time, wasted resin, and weld line are adopted as objective functions to be minimized for optimization. The correlation among objective functions and design rule of gate location are extracted using a clustering approach known as a self-organizing map (SOM).²⁴ This manuscript is organized as follows. Section Numerical Procedure describes the details of the numerical method of the void-formation model, resin filling simulation, and MOO. Section Experiment Method discusses the experimental procedure for extracting the inherent characteristics of the filling simulation and validating the void-formation model as a radial injection. Section Result and Discussion presents the results and a discussion, demonstrating the efficiency of our developed framework, and extracting the correlations among objective functions and the design rule of the arrangement of injection positions.

Numerical procedure

We combined a numerical simulation with an existing void-formation model proposed by Park et al.¹² The finite-element/control-volume (FE/CV) method is used to simulate flow advancement, and it is combined with the void-formation model. We used four node isoparametric quadrilateral elements for FEM model. In the following, we describe the procedure for the filling simulation and the void-formation model. Additionally, this section introduces the optimization procedure. We used our original in-house codes for both flow advancing simulation and MOO.

RTM filling simulation

In RTM, resin impregnates fabric at low speed (the Reynolds number is usually much less than 1). Therefore, resin flow can be described by Darcy's law. Since woven fabrics have dual-scale pores (inter- and intra-bundle), we considered two flow paths in a unit cell model, which is illustrated in Figure 1. The red line indicates the inter-bundle flow path, and the blue line indicates the intra-bundle flow path. As mentioned in the previous section, inter-bundle flow can be expressed as usual by Darcy's law; however, in intra-bundle flow the capillary effect should be considered, because of the small gap between fiber filaments. Therefore, resin flow

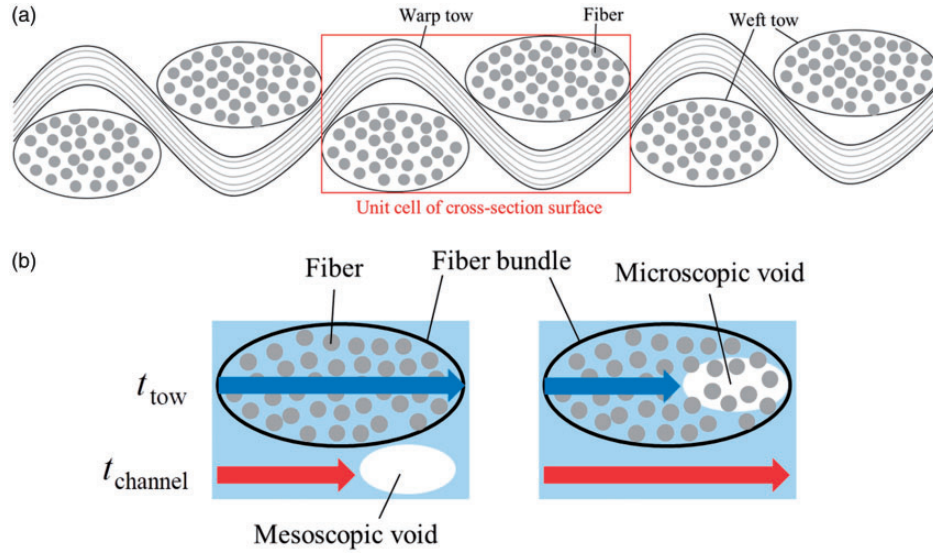


Figure 1. (a) Simulation unit cell of woven fabric. (b) Schematic diagrams of void formation models.

velocity for each flow path can be expressed as the following equations^{19,21}

$$U = -\frac{K_n}{(1 - V_{f,c})\mu} \nabla P_n \quad (2)$$

$$u = -\frac{K_T}{(1 - V_{f,t})\mu} \left(\nabla P_T - \frac{P_{cap}}{l} \right) \quad (3)$$

where U is the resin velocity in the resin impregnation direction, $V_{f,c}$ is the fiber volume fraction, K_n is the permeability of fabric in the resin impregnation direction, ∇P_n is the pressure gradient of the impregnation direction, u is the resin velocity inside the fiber bundle, K_T is the permeability of the fiber bundle as defined by each fiber direction, $V_{f,t}$ is the fiber volume fraction of the fiber bundle, ∇P_T is the pressure gradient decomposed into each fiber direction, and P_{cap} is the capillary pressure. l is the length of the fiber bundle, and we used constant values for l with weft and warp directions.¹² These values are listed as “L” and “W” in Table 2. To obtain the pressure and velocity distributions in the analytical model, equation (2) was coupled with the continuity equation for an incompressible fluid (i.e. the divergence of the velocity is zero). The coupled equation was solved under the following boundary conditions

$$\begin{aligned} P &= P_0 \text{ at the resin inlet} \\ P &= 0 \text{ at the flow front} \\ \frac{\partial P}{\partial n} &= 0 \text{ at the mold wall} \end{aligned} \quad (4)$$

Here, P is the resin pressure, P_0 is the prescribed injection pressure, and $\frac{\partial P}{\partial n}$ is the pressure gradient

perpendicular to the mold wall. Details of the numerical procedure are given in our previous paper.²⁵ The impregnation direction of the resin flow can be determined using equation (5)

$$\alpha = \tan^{-1} \left(\frac{U_y}{U_x} \right) \quad (5)$$

where α is the impregnation angle of the resin, U_y is the y-axis velocity, and U_x is the x-axis velocity. This angle is used to determine the decomposed pressure gradient used in equation (3), and ∇P_T can be calculated from the pressure gradient of the impregnation direction using equation (6)

$$\begin{aligned} \nabla P_T &= \nabla P_n \cos \alpha \quad (\text{for warp direction}) \\ \nabla P_T &= \nabla P_n \sin \alpha \quad (\text{for weft direction}) \end{aligned} \quad (6)$$

The capillary pressure that appears in equation (3) is expressed as¹²

$$P_{cap} = \left(\frac{F}{d_f} \right) \frac{V_{f,t}}{1 - V_{f,t}} \gamma \cos \theta \quad (7)$$

where F is a shape factor determined by the experiment and d_f is the fiber filament diameter. The impregnation times for both flow paths can be obtained by integrating equations (2) and (3) over time, as expressed below

$$\Delta T = \frac{L}{\frac{1}{1 - V_{f,c}} \cdot \frac{K_n}{\mu} \cdot \nabla P_n} \quad (8)$$

$$\Delta t = \frac{l}{\frac{1}{1 - V_{f,t}} \cdot \frac{K_T}{\mu} \cdot \nabla P_T} \left[1 + \frac{P_{cap}}{l \cdot \nabla P_T} \ln \left(1 - \frac{l \cdot \nabla P_T}{P_{cap}} \right) \right] \quad (9)$$

Here, ΔT is the travel time for the inter-bundle path, L is the length of the inter-bundle path, and Δt is the travel time for the intra-bundle path. The presence of voids is determined from the time difference between the two flow paths and will be discussed in detail in the next section.

Void-formation model

This section presents a brief overview of the void-formation model proposed by Park et al.¹². The difference in travel times of the flow between inter- and intra-bundle regions determines the volume fraction of mesoscopic or microscopic voids. Figure 1(b) presents a schematic diagram of these formations for mesoscopic and microscopic voids. When the travel time of the inter-bundle flow calculated by equation (8) is shorter than that in the fiber bundle calculated by equation (9), voids form in the fiber bundle (microscopic voids). In contrast, voids between fiber bundles (mesoscopic voids) form in the opposite case. The unimpregnated area is considered to be proportional to these time differences. If the total flow does not coincide with the orientation of the fiber bundle, the pressure gradient must be decomposed in the longitudinal and transverse directions with respect to the fiber bundle. Based on these assumptions, mathematical formulations for the void-formation model are given below.

$$\begin{aligned}\Delta t_{T,wp} &= \min[\Delta t_{x,T,wp}, \Delta t_{y,T,wp}] \\ \Delta t_{C,wp} &= \min[\Delta t_{x,C,wp}, \Delta t_{y,C,wp}]\end{aligned}\quad (10)$$

Here, the void fractions for the warp are formulated. The impregnation time in the warp and the flow time in the channel region along the warp are determined as follows

When $\Delta t_{T,wp} > \Delta t_{C,wp}$, microscopic voids form and the portion of unimpregnated region is estimated by

$$\Phi_{T,wp} = h_{v,T,wp} \cdot \left(1 - \frac{\Delta t_{C,wp}}{\Delta t_{x,T,wp}}\right) \cdot \left(1 - \frac{\Delta t_{C,wp}}{\Delta t_{y,T,wp}}\right)\quad (11)$$

where $h_{v,T,wp}$ is a structure factor of microscopic voids, which is determined by observation of voids. For $\Delta t_{T,wp} < \Delta t_{C,wp}$, mesoscopic voids form, and the portion of unimpregnated region is estimated by

$$\Phi_{C,wp} = h_{v,C,wp} \cdot \left(1 - \frac{\Delta t_{T,wp}}{\Delta t_{x,C,wp}}\right) \cdot \left(1 - \frac{\Delta t_{T,wp}}{\Delta t_{y,C,wp}}\right)\quad (12)$$

where $h_{v,C,wp}$ is a structure factor. Equations (11) and (12) give the volume fraction of voids, which is proportional to

the difference between impregnation times in the inter- and intra-bundle regions. Using almost the same formulations, the portion for the weft can also be estimated.

Finally, the void fractions for mesoscopic and microscopic voids are estimated by considering the volume fraction of a tow for a unit cell and that of a fiber for a tow. The mesoscopic void fraction emerging in the inter-bundle region is obtained as

$$V_{a,C} = \frac{\Phi_{C,wp} \cdot v_{wp} + \Phi_{C,wt} \cdot v_{wt}}{v_{wp} + v_{wt}} (1 - v_{wp} - v_{wt})\quad (13)$$

where v_{wp} is the volume fraction for warp and v_{wt} is that for weft. In contrast, the microscopic voids inside tow regions are represented by

$$\begin{aligned}V_{a,wp} &= \Phi_{T,wp} \cdot v_{wp} \cdot (1 - V_{f,wp}) \\ V_{a,wt} &= \Phi_{T,wt} \cdot v_{wt} \cdot (1 - V_{f,wt})\end{aligned}\quad (14)$$

where $V_{f,wp}$ is the fiber volume fraction for warp and $V_{f,wt}$ for weft. Our study investigated void fractions calculated using equations (13) and (14). However, some additional considerations are necessary to reproduce the actual void formation process in RTM. Compression of voids is an especially important phenomenon. In this study, the compression phenomenon during void formation is also implemented, and the void fractions obtained by equations (13) and (14) are improved to better values. The formulation of the compression phenomenon is described below.

The compression phenomena of voids occur under the influence of the resin pressure around them. They are considered for both mesoscopic and microscopic voids and are calculated in different procedures. Once formed at the flow front of the resin, mesoscopic voids continue to be compressed over time, due to the resin pressure around them. When the temperature of the resin is constant, the mesoscopic void fraction can be updated by considering the law of ideal gas as follows

$$V_{a,C}(x, y, t + \Delta t) = \frac{P(x, y, t)}{P(x, y, t + \Delta t)} V_{a,C}(x, y, t)\quad (15)$$

where Δt is a time step.

After microscopic voids form in the fiber bundle, they are compressed not only by the surrounding resin but also by the capillary pressure generated in the fiber bundle. The capillary pressure has a considerable effect on the surrounding resin flow and causes resin flow into the fiber bundle when the microscopic voids are compressed. Since the actual cross-section of the fiber bundle is elliptical (Figure 2), only the thickness direction of the resin flow into the fiber bundle is considered (the flow in the planar direction is ignored).

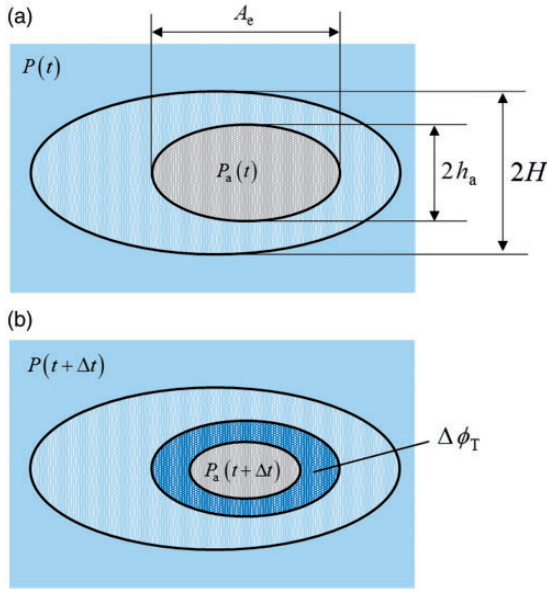


Figure 2. Schematic diagrams of microscopic void compression. (a) Before compression. (b) After compression.

The resin flow in the thickness direction into the fiber bundle can be obtained from Darcy's law as follows

$$u_{tr} = \frac{K_T}{\mu} \frac{P - P_a + P_{cap}}{H - h_a} \quad (16)$$

where u_{tr} is the resin flow velocity in the thickness direction, P_a is the air pressure in the microscopic void, H is the thickness of the fiber bundle, and h_a is the thickness of the microscopic void. Here, h_a is approximated as follows using the portion of unimpregnated region ϕ_T obtained by equation (11)

$$h_a = H \cdot \phi_T \quad (17)$$

Also, if the ideal gas law is applied, the pressure in the microscopic voids can be obtained as follows

$$P_a(t + \Delta t) = \frac{\phi_T(t)}{\phi_T(t + \Delta t)} P_a(t) \quad (18)$$

The portion of unimpregnated region after the time step Δt , $\phi_T(t + \Delta t)$, is calculated by updating as follows

$$\phi_T(t + \Delta t) = \phi_T(t) - \frac{2 \cdot u_{tr} \cdot A_e \cdot \Delta t}{(1 - V_f) \cdot (l_{long} \cdot l_{tran} \cdot H)} P_a(t) \quad (19)$$

where l_{long} is the length in the longitudinal direction of the fiber bundle and l_{tran} is the length in the transverse

direction. Here, A_e is the effective area of the impregnated region and is approximated as

$$A_e = l_{long} \cdot l_{tran} \cdot \phi_T(t) \quad (20)$$

These calculations are performed for warp and weft. After updating the portion of the unimpregnated region using equation (19), the microscopic void fraction after compression is calculated by applying equation (14). The compression is repeated until the sum of the surrounding resin pressure and the capillary pressure within the fiber bundle is less than the pressure within the microscopic void.

Multi-objective optimization

In this study, the MOO problem was solved using a genetic algorithm (GA). Since GA is a population-based optimization approach, the possibility of converging to a local optimum solution is lower than with a gradient-based method. Therefore, many previous studies adopted GA to optimize the injection locations.^{25–28} The values of the objective functions are calculated for all sets of injection points obtained from the multi-objective GA (MOGA). In this optimization, we considered four objective functions: fill time, weld line, total void fraction (total fraction of mesoscopic and microscopic voids), and wasted resin. These four objective functions are defined in FEM simulation as follows. Fill time is the time required to fill all nodes with resin. In flow advancing simulation in CV/FEM model, the length of weld line is calculated by $(The\ length\ of\ weld\ line) = \sum_i f_i \cdot V_i$, where i is the node number, f is the fill fraction of resin, and V is the area of the control volume element.²⁵ When two flow fronts simultaneously fill node i with opposite directions, we added value of $f_i \cdot V_i$ to the length of weld line. Total void fraction is defined as the average mesoscopic void and microscopic void fractions of the analytical model domain obtained using equations (13) and (14). Wasted resin is the quantity that bleeds out from the prescribed vent nodes. Based on our previous study,²⁵ the dry spot is proportional to the wasted resin; therefore, the dry spot is not added to the objective function. In addition, solutions with more than 1% dry spots are eliminated as candidates for Pareto solutions. Hence, the obtained Pareto solutions have few dry spot areas. In this case, all objective functions should be minimized to optimize the process conditions. Since there are four objective functions, it is difficult to find an optimal solution that is superior to other solutions in terms of all objective functions. Thus, in this study Pareto solutions are sought instead. A Pareto solution is defined as a solution in which one objective function cannot be improved without

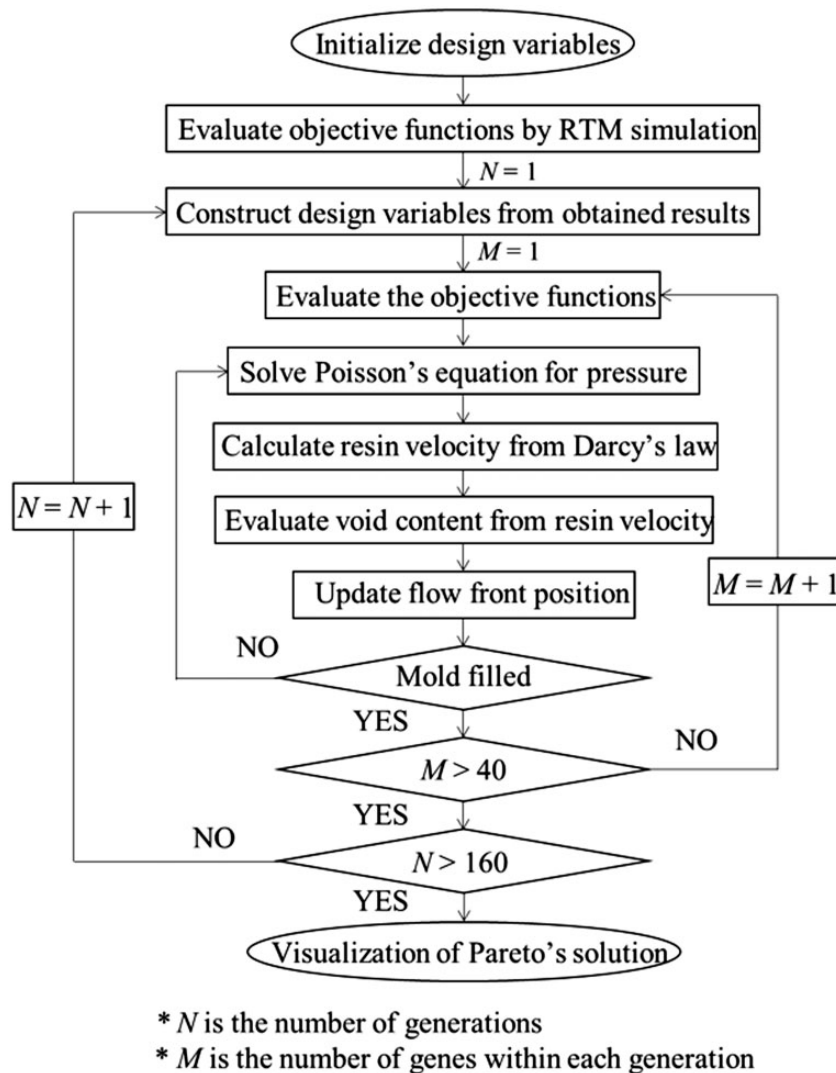


Figure 3. Flowchart of filling simulation with optimization.

degrading other objective functions and there are no other solutions that are superior in all objective functions. To find the Pareto solutions, a Pareto ranking method was used. With this method, all solutions are ranked as follows

$$\text{rank}(i) = 1 + n \quad (21)$$

where i is the solution number and n is the number of other solutions that are superior to the ranked solution in all objective functions. A solution having rank = 1 is regarded as a Pareto solution.

The design variables of the MOO problem are the two injection locations, and an FEM element is used to express the gate (i.e. the injection radius is equal to the element size). Therefore, variation range in gate location is same as element size. Figure 3 presents a flowchart of our simulation. As shown in the figure, we

obtained Pareto solutions of injection location by calculating GA and resin-filling simulation alternatively. We used GA through a real-encoded algorithm.²¹ This algorithm gives us optimized injection locations as continuous coordinates. On the other hand, an injection location for resin filling simulation is positioned at the center of an element in FEM model, and can take position discretely. For the gate of the resin-filling simulation, we selected the element that has the closest position to the optimized injection location. Therefore, slight differences exist between the obtained design variables and the simulated injection locations. However, we consider these differences to be small enough to neglect. For the parameters in MOGA, the crossover rate was 1.0, and the mutation rate was 0.1. The crossover and the mutation processes generate optimized injection locations both inside and outside the model. We rejected injection location outside the system to

avoid unrealistic solution. We continued the MOGA until we reached 150 generations. In each generation, 40 new genes were added. Figure 3 presents a flowchart of our simulation.

Experiment method

In this study, we conducted an RTM experiment and molded FRP in addition to analytical investigations. The two purposes of the experiment were determination of the permeability of the global flow for fiber preform and qualitative validation of the distribution of the void fraction for molded FRP. In this section, we discuss the setup of equipment for the RTM experiment, the method to determine permeability, and the procedure to observe voids.

Resin injection experiment and determination of permeability

To determine the permeability for global flow, we conducted one-point radial injection in fabric. Figure 4(a) is a schematic diagram of the experiment apparatus, and Figure 4(b) is a photograph of the mold that was actually used. There is a gate at the center of the mold, and a vent is provided near the corner of the mold. The mold consisted of two 25 cm × 25 cm transparent glass plates and two plates were connected using a sealant tape to seal the inside of the mold. Before sealing the mold, it was necessary to place the fiber preform as reinforcement for FRP in the mold (preforming). In this study, we adopted a plain-woven glass fiber preform as reinforcement; it was cut into 18 cm × 18 cm so as to match to the size of the mold. Glass fiber preforms have been used in many studies that conducted permeability measurement experiments.^{29–31} A commercially available polyester resin was set on the gate side after mixing with a suitable curing agent.

To inject the resin, the pressure inside the mold must be lower than the pressure at a gate. Therefore, in this study, a vacuum pump was connected to the vent side, and negative pressure was applied to the mold to generate a pressure gradient. A regulator was connected between the vacuum pump and the vent, and the negative pressure was set at 50 kPa, which is the same as the injection pressure that we applied in the simulation. The resin was then injected under constant pressure. This experiment was performed at room temperature (298 K) so as to delay curing of the resin.

To determine the permeability, it is necessary to track the advancement of the flow front position of the resin with the lapse of time. Using a transparent glass plate for the mold, we can capture the behavior of the resin in the mold using a video camera set at the top of the mold. From the relationship between the

time and the flow front position taken by the video camera, permeability is calculated by the following equation³²

$$K_n = \frac{\mu(1 - V_f)}{4t\Delta P} \left[x^2 \left\{ 2 \ln \left(\frac{x}{r} \right) - 1 \right\} + r^2 \right] \quad (22)$$

where K_n is the permeability in the global flow, t is the elapsed time, x is the distance from the gate, and r is the injection radius. Immediately after the start of injection, the calculated permeability is unstable; however, its value becomes almost constant as time elapses. The permeability measured in the experiment is used for the filling simulation.

Observation of mesoscopic voids

After performing the resin injection experiment, the resin impregnated in the fiber preform cured at room temperature. In the case of RTM, it means that molding of FRP is completed at the time when curing of the resin is completed. After curing, the molded glass fiber reinforced plastic (GFRP) is removed from the mold. In the mesoscopic void observation, we used digital-microscope (model VH-5500; Keyence Co. Ltd., Osaka). The window size is 2.95 mm × 2.36 mm. In order to observe voids generated by the air entrapment, the surface of GFRP was observed. However, it is difficult to examine all void distributions in GFRP. Figure 4(c) represents observation points at 10 mm, 30 mm, and 50 mm from injection point for warp and weft directions.

Result and discussion

Numerical test for distributions in mesoscopic and microscopic voids by unidirectional flow

To verify the validity of our numerical analysis, RTM filling simulation for simple unidirectional flow was carried out. In the model shown in Figure 5(a), element size is (12.5 mm)² and total element number is 3200. Unidirectional flow was realized by replacing all elements at the left edge of the simulation model with gates and those at the right edge with vents. The distance between gate and vent was set to 1 m. Table 1 lists the material properties used for resin, and Table 2 lists those for fabric. Figure 6 plots the relationship between the void fraction and the distance from the gate obtained by our analysis Figure 6(a) and analysis by Park et al. Figure 6(b).¹² Several parameters (e.g. permeability) used in our analysis were obtained by fitting in order to conform to the analysis conditions of the thesis.¹² Our results are in good agreement with those of Park et al.

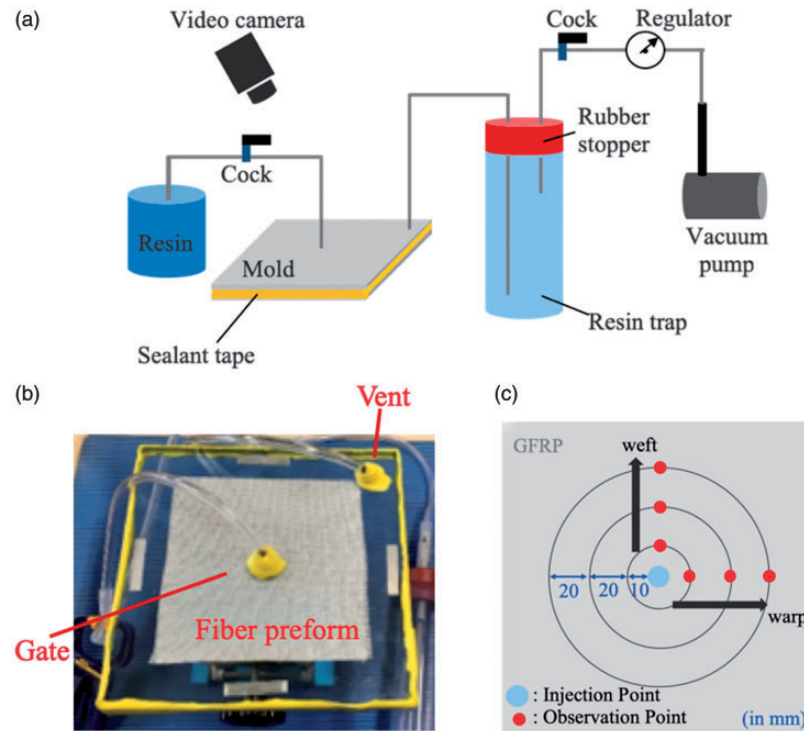


Figure 4. (a) Schematic diagram of the set-up of the RTM experiment. (b) Picture of mold. (c) Schematic diagram of the observation points of a mesoscopic void. RTM: Resin transfer molding.

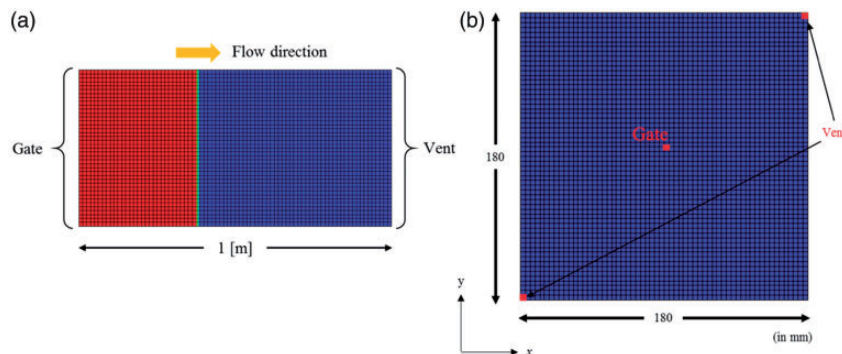


Figure 5. Simulation models of filling simulation. (a) Rectangle model for uniaxial injection. (b) Square model for radial injection.

Our results (Figure 6) provide us with some important suggestions for void formation. First, no mesoscopic voids are generated near gates, because the global flow near the gate is faster than the flow in the intra-bundle. As the distance from the gate increases, the global flow becomes slower and the flow in the intra-bundle becomes faster. As a result, mesoscopic voids form between the fiber bundles. However, many microscopic voids are generated near the gate, and void fraction decreases as distance from the gate increases. This is because the flow in the intra-bundle is slow near the gate, and air is confined in the intra-bundle. These results confirm that the sum of the mesoscopic void

fraction and the microscopic void fraction is the smallest in the vicinity midway between the gate and the vent. In fact, the minimum total void fraction is obtained 0.6 m from the gate. At that value, it is assumed that the global flow velocity is close to the flow velocity in the intra-bundle.

To obtain more general insight that does not depend on system size, the relationship between the general modified capillary number expressed by equation (1) and the void fraction was investigated. Figure 7 plots the relationship between the modified capillary number and the void fraction. As the modified capillary number increases, microscopic voids increase and mesoscopic

Table 1. Resin properties used in this study.

Density ρ (kg/m ³)	1100
Viscosity μ (Pa·s)	0.15
Surface tension γ (N/m)	0.0317
Contact angle θ (degree)	30

Table 2. Fabric properties used in this study.

Fiber volume fraction of preform ρ_f (%)	58
Fiber volume fraction inside warp bundle $V_{f,wp}$ (%)	64
Fiber volume fraction inside weft bundle $V_{f,wt}$ (%)	64
Warp volume fraction $v_{f,wp}$ (%)	45.3
Weft volume fraction $v_{f,wt}$ (%)	45.3
Fiber diameter d_f (m)	1.4×10^{-5}
Longitudinal length of bundle L (m)	5.5×10^{-3}
Transverse length W (m)	4.5×10^{-3}
Height of bundle H (m)	5.0×10^{-4}
Global permeability of perform for x direction K_x (m ²)	7.0×10^{-11}
Global permeability of perform for y direction K_y (m ²)	3.0×10^{-11}

voids decrease; their magnitude relationship reverses at 0.0004. Since the order of the value is consistent with the results published in many previous studies, we can confirm again that this numerical simulation can accurately reproduce void formation.

Analysis of the distribution of mesoscopic and microscopic voids using one-point radial injection

Measurement of permeability in an RTM experiment. Measurement of permeability in an RTM experiment was performed three times. The part impregnated with resin is symmetrical, so the vent position does not influence the direction of resin flow. Table 3 lists the results for warp direction and weft direction. Permeability in the warp direction differ from that in the weft direction. The difference in permeability is mainly due to the anisotropy of the glass fiber mat. The thickness of the fiber bundle differs between the weft and warp directions, which causes the permeability difference. Errors between the average value and the measured value are within 15%, which is within the allowable range. A subsequent simulation was carried out using these average permeability values.

Prediction of the distribution of void fractions using numerical simulation. In this section, void distribution is investigated for one-point radial injection in plain-woven fabric. The material properties are the same as those

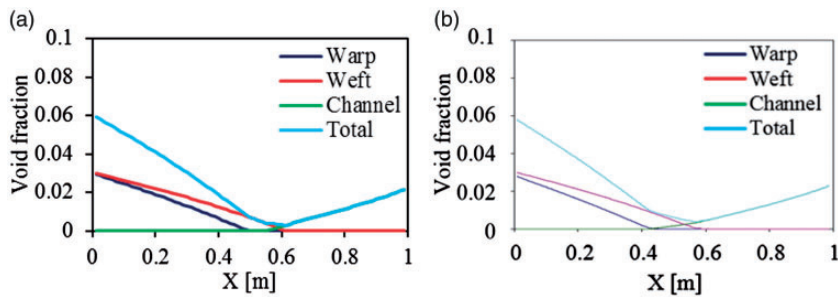


Figure 6. Void fraction vs. distance from the gate. (a) This simulation. (b) Park et al.¹²

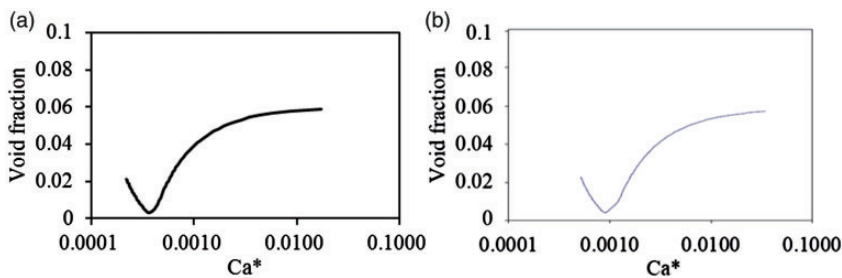


Figure 7. Void fraction vs. modified capillary number. (a) This simulation. (b) Park et al.¹²

Table 3. Global permeability obtained by RTM experiments of one-point injection.

	K_x (m^2)	K_y (m^2)	Error (%) (K_x)	Error (%) (K_y)
1	2.10×10^{-11}	5.33×10^{-12}	11.89	14.93
2	2.05×10^{-11}	4.65×10^{-12}	9.23	9.23
3	1.66×10^{-11}	4.21×10^{-12}	-11.50	-11.50
Average value	1.94×10^{-11}	4.73×10^{-12}	-	-

RTM: resin transfer molding.

in the above simulation (Tables 1 and 2), except for the global permeability of the preform, which is adapted as an experimental value. In the simulation of one-point radial injection RTM, Figure 5(b) represents a square model with a side of 180 mm, which is the same size as that in our experiment. The size of each element is $(3 \text{ mm})^2$. The number of elements of the FEM simulation is 3600, and the number of nodes is 3721. To match the experiment conditions, resin was injected from the center of the model, the boundary conditions for the gate were imposed on the nodes corresponding to the injection radius of 3 mm, and the vacuum pressure was set at 50 kPa. The element at the upper right vertex of the model was set to vent. Figure 8 illustrates the distributions of void fractions for mesoscopic and microscopic voids obtained by numerical simulation. In this figure, red indicates higher void fractions and blue indicates lower ones. One key feature in this figure is similar to the result obtained in unidirectional flow: the mesoscopic void fraction increases when the distance from the gate increases, whereas the opposite is true for the microscopic void. This feature is consistent with previous experiment studies.¹¹

Since a constant-pressure injection strategy is applied to the gate, the negative pressure gradient decreases with the advance of the flow front. Based on equation (2), resin velocity is proportional to pressure gradient; thus, decrease in the pressure gradient is related to low resin velocity. Near the gate, pressure gradient was higher and the viscous force was dominant in void generation; however, a low-pressure gradient was found near the wall, and the capillary effect became dominant in this area. If the capillary force is dominant, the flow in the intra-bundle is faster than that in the inter-bundle; consequently, mesoscopic voids occur. Therefore, the fraction of mesoscopic voids increases with an increase in distance. With one-point injection in the bulk case (the boundary of the system is not considered), the distance from the gate point is essential for void distribution. In contrast, with multi-gate injection in a system with a boundary, void distributions are assumed to be affected by both

distance and gate arrangement in the system because of acceleration of the flow due to conjunctions initiated at the gates. In the following section, optimum (two) gate positions are investigated using the MOO method where flow analysis is combined with GA.

Observation of void in GFRP. To validate the simulated distribution of mesoscopic voids, Figure 9 depicts the surfaces of molded GFRP at the observation points in Figure 5(c). There is no mesoscopic void near the gate for both warp and weft directions (left figures). However, mesoscopic voids increase with distance from the injection point (center and right figures). Furthermore, more mesoscopic voids are observed in the weft direction than in the warp direction. The distance and orientation dependences of void formation are consistent with our simulation result (Figure 8(a)). Therefore, our simulation can qualitatively reproduce the experiment. In this study, we observed only mesoscopic void content. In order to obtain distribution of microscopic void distribution, we have to observe the microstructure of the specimen with high resolution method, such as X-ray computed tomography.³³ To observe microscopic void is one of our future tasks.

Gate optimization for two-point injection

The optimum gate position for RTM with the two-point injection is determined by the MOO constructed in section Multi-objective optimization. As depicted in Figure 5(b), two vents were placed at two-edge elements in the diagonal direction. The design variables and objective functions of the MOO problem are introduced in Section Multi-objective optimization. The material properties are listed in Tables 1 and 2, and the permeability and the vacuum pressure are the same as those for the one-point injection described above. First, convergence of the optimization in GA was checked. Figure 10 plots the relationship between fill time and weld line for each generation. The black dotted curve indicates the Pareto front over 150 generations. This figure indicates there are few Pareto front movements from 100 generations to 150 generations; thus, the Pareto front has achieved convergence at 150 generations. Hence, our optimization sufficiently converged, and 150 generations were selected as the maximum number of calculated generations for this optimization.

Figure 11 presents a scatter-plot matrix of 192 Pareto solutions obtained from the optimization result. The values in this figure indicate Pearson's coefficient, which represents the strength of correlation, and the graphs present the correlation diagrams for each objective function. As Pearson's coefficient approaches 1, the relationship between two objective functions

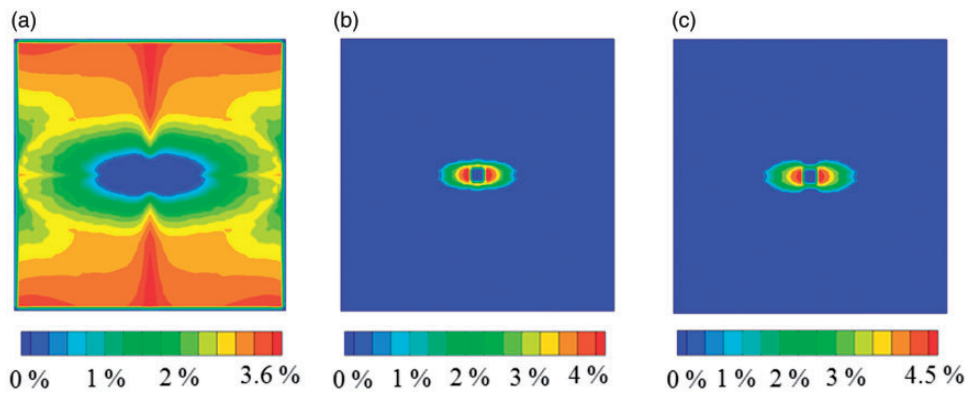


Figure 8. Distributions of each void for radial injection. (a) Mesoscopic void. (b) Microscopic void (warp). (c) Microscopic void (weft).

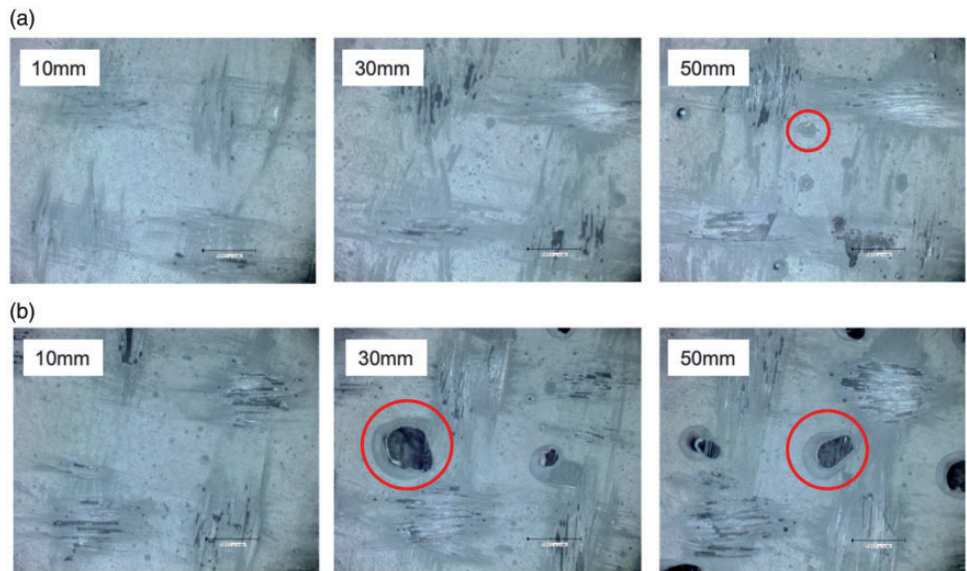


Figure 9. Observations of mesoscopic voids at different distance from the injection point. Figures from left to right are at 10 mm, 30 mm and 50 mm for (a) warp and (b) weft directions. Red circles denote representative mesoscopic voids.

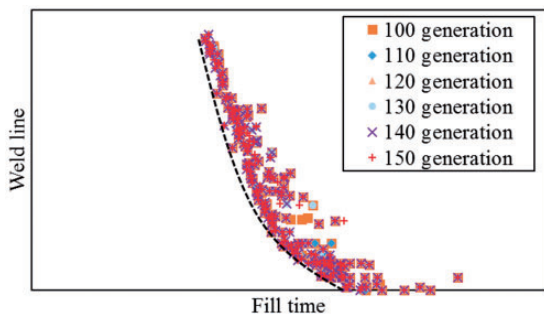


Figure 10. Pareto solutions movement with respect to generations.

Fill time			
-0.89	Weld line		
0.78	-0.70	Total void	
0.62	-0.35	0.22	Wasted resin

Figure 11. Scatter plot matrix of objective functions. (Values indicate Pearson's correlation coefficient.)

exhibits strong positive correlation; in contrast, as it approaches -1 , the relationship exhibits strong negative correlation. A positive correlation was found between fill time and wasted resin. Since wasted resin is analyzed as the scalar product of the time and flow rate in vent nodes, any increment of fill time causes resin bleeding. Hence, these relationships obtained from optimization are reasonable. Fill time and total voids also had a positive correlation, because the global flow velocity at the flow front decreases as time passes, causing the formation of mesoscopic voids. In contrast, negative correlations were found between the weld line and total voids, and between fill time and weld line. These negative correlations suggest trade-off relations that lead not to global solution but to Pareto solutions.

To extract more detailed information about the optimization results, Pareto solutions in gate arrangements are clustered using SOM.

Figure 12(a) is an SOM-Ward cluster figure of three clusters, and their representative gate positions are drawn on the map of each cluster. All representative gate positions are arranged diagonally opposite to the vent. These differences are only the distances between the gates, and this distance is increased in the order of cluster 2, 1 and 3. Figure 12(b) plots the parallel coordinates that correspond to each cluster, and normalized values of the objective functions are indicated on the y-axis. Detailed characteristics in each cluster are summarized as follows. In cluster 1, all objective functions have relatively average values. In cluster 2, the weld line

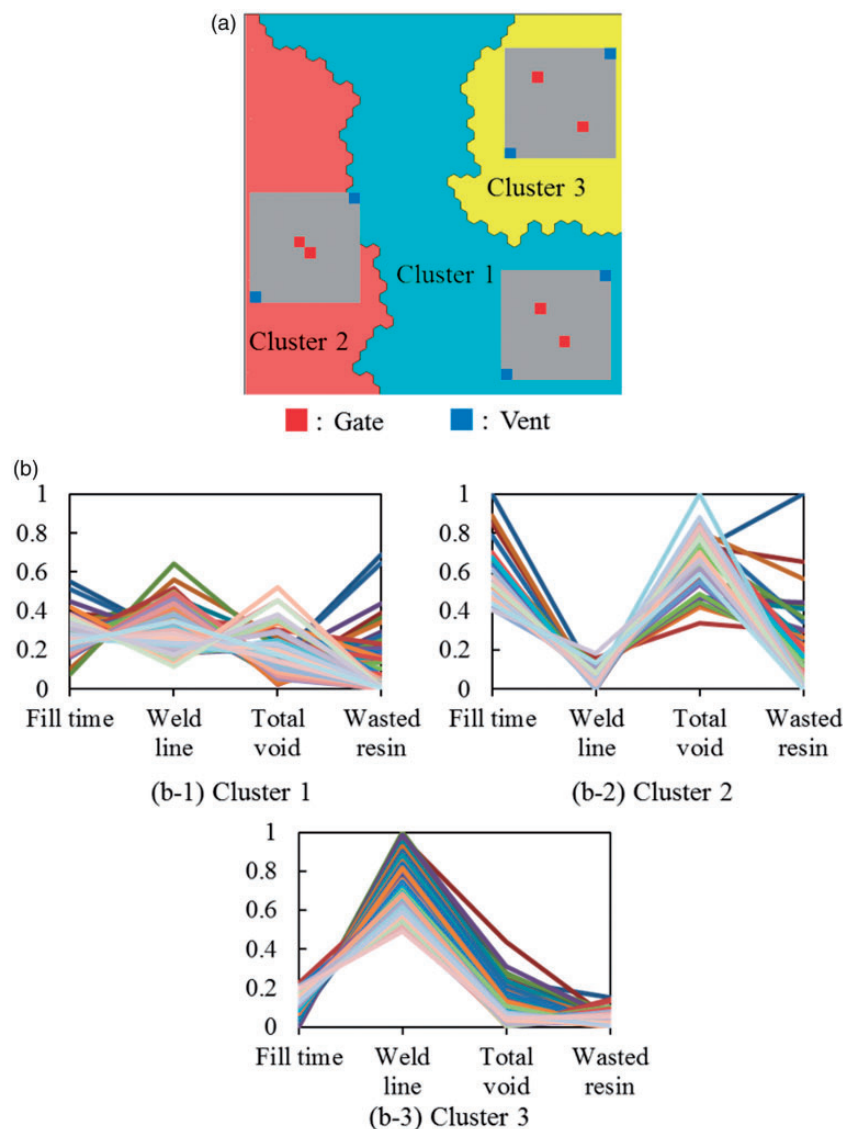


Figure 12. Results of MOO calculations: (a) SOM-ward of Pareto solutions with representative gate arrangements. (b) Parallel coordinates for each cluster.

MOO: multi-objective optimization; SOM: self-organizing map.

is optimized at the expense of the fill time and the total voids. In cluster 3, the fill time, wasted resin, and total voids are superior, although the weld line has a higher value. The characteristics in these clusters correspond to the relations obtained using the scatter-plot matrix.

Based on Figure 12(a) and (b), the relationship between gate location and objective function is obtained. If the distance between two gates is short (e.g. Figure 12(b) cluster 2), the weld line tends to be short, and a longer fill time and a greater total void fraction are found. For the multi-injection model, the following conditions are generally required to reduce the fill time and the wasted resin simultaneously. First, each gate equally occupies the region (i.e. the perpendicular bisector of the straight line connecting the two gate positions divides the system area

equally). Next, each gate is located at the center of gravity of the region. Without considering flow conjunction from two different injection points, the first condition is sufficient to reduce the wasted resin; however, the second condition is also necessary to reduce the fill time. Clusters 1, 2, and 3 satisfy the first condition. Clusters 3, 1, and 2 are close to the second conditions in that order, and the representative gate position in cluster 3 is excellent with respect to fill time. A weld line is defined as a region where two flow fronts collide, and it is inversely proportional to gate distance. Therefore, from the viewpoint of the distance between gates, a trade-off relationship can be obtained between weld line and fill time. The following section discusses the relationship between gate arrangement and each void considering flow conjunction.

Figure 13 illustrates the spatial distributions of mesoscopic and microscopic voids for a representative gate arrangement of each cluster. The features observed by comparing clusters 1, 2, and 3 are summarized as follows. Mesoscopic void increases in order of the closeness between gates, whereas microscopic void does not depend on the distance between gates. Only when the distance between gates is sufficiently small is the microscopic void clearly reduced by overlapping of voids that emerged from different injection points. When two gate positions are independently located in the system, resin flow velocity increases due to the joining of the resins, which also leads to reduction of mesoscopic voids. Therefore, the total amount of mesoscopic

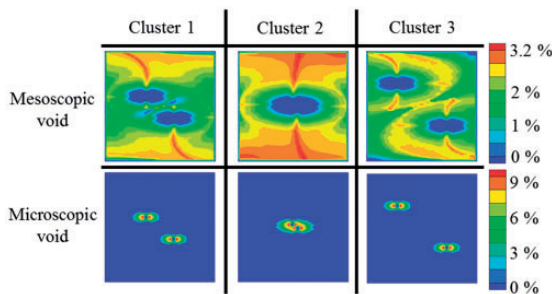


Figure 13. Distribution of mesoscopic and microscopic voids.

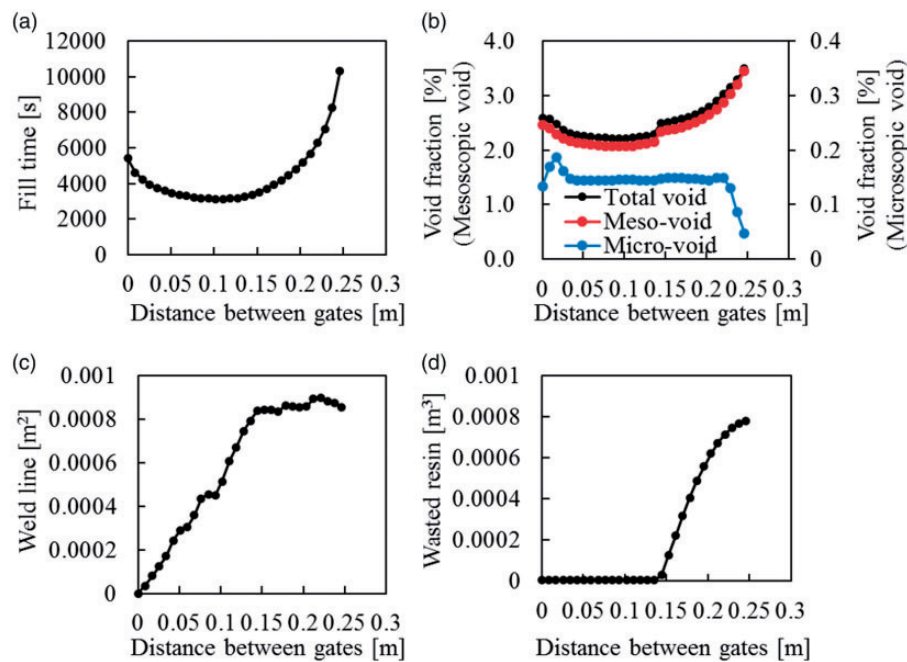


Figure 14. Objective function vs. distance between gates.

and microscopic voids is not a simple proportional relationship with respect to distance, and there seems to be an appropriate distance to optimize the objective functions.

Each objective function in MOO was investigated when the distance between gates was changed while keeping the diagonal arrangement. Figure 14 plots the relationship between the two-gate distance and each objective function. The optimum distance with respect to fill time, total void fraction, and wasted resin is from 0.1 m to 0.15 m. When each gate position is located at the center of gravity of each region of a whole system, the distance is 0.126 m, which corresponds to our obtained distance. Hence, to minimize fill time, wasted resin, and total void simultaneously, the gate position at the center of gravity of the two areas divided by the line connecting vents is regarded as the reference for appropriate molding. Flow conjunction is assumed to change the appropriate distance slightly from 0.126 m, due to the increase of flow speed and decrease of mesoscopic voids. However, when considering weld line and wasted resin, one injection location at the center of a mold is the appropriate condition, although the mesoscopic void becomes large. In conclusion, a diagonal arrangement with an appropriate distance is required for appropriate molding depending on polymer resins. Finally, it should be noted that this study evaluated a quality of a product only by total void content and weld line for simplification. However, previous studies reported that not only total void content but also void localization, void location, and void shape are important for the quality.^{34,35} This point will be studied in the near future.

Conclusion

This study proposed a simulation-based MOO framework of RTM for a woven fabric, and observed the void distribution to validate the proposed approach. This framework was realized by combining MOGAs and flow dynamics simulation including microscopic and mesoscopic void formations, which are inherent phenomena in molding inside woven fabric. First, we verified the void-formation model by conducting unidirectional flow simulation. The calculated void fractions almost agreed with the previous results by the authors who proposed the void-formation model. Next, the experiment and the numerical simulation for one-point radial injection were performed. Our experiment extracted the permeability of GFRP as a parameter for the filling simulation. Furthermore, observation successfully captured features of void distribution. (1) The mesoscopic void in the warp direction is smaller than that in the weft direction. (2) The mesoscopic void increases with distance from the injection point.

These results qualitatively guarantee the accuracy of our simulation. Finally, MOO was demonstrated for the flat plate model with two vents at diagonal corners of the system. Our result confirmed trade-off relationships of weld line with fill time, wasted resin, and total amount of void; however, we found positive correlations among fill time, total void fraction, and wasted resin. Furthermore, SOM extracted the design role for optimum injection locations (i.e. the arrangement of two gates on the perpendicular bisector of the straight line connecting the vents is appropriate for all molding characteristics). This arrangement does not seem to depend on the permeability ratio between two perpendicular directions of the preform. We also found that the distance between two injection locations has a significant effect in minimizing mold characteristics. The results obtained above will be useful for optimum mold design in actual RTM of a woven fabric-reinforced composite in the future. This study investigated only the flat plate model; however, our framework and results will help determine optimum molding conditions even in complicated shape molding.

Declaration of Conflicting Interests


The author(s) declared no potential conflicts of interest with respect to the research, authorship, and/or publication of this article.

Funding

The author(s) disclosed receipt of the following financial support for the research, authorship, and/or publication of this article: The Cross-Ministerial Strategic Innovation Promotion Program and the Ministry of Education, Culture, Sports, Science and Technology of Japan under Grant-in-Aid Scientific Research (C) No. 15K06597. Toray Industries, Inc. also supported this work.

ORCID iDs

Yutaka Oya  <https://orcid.org/0000-0003-2136-6004>

Ryosuke Matsuzaki  <https://orcid.org/0000-0001-8237-1638>

References

1. Soutis C. Carbon fiber reinforced plastics in aircraft construction. *Mat Sci Eng A* 2005; 412: 171–176.
2. Pillai KM and Advani SG. Numerical simulation of unsaturated flow in woven fiber preforms during the resin transfer molding process. *Polym Compos* 1998; 19: 71–80.
3. Pillai KM. Governing equations for unsaturated flow through woven fiber mats. Part 1. Isothermal flows. *Compos A Appl Sci Manuf* 2002; 33: 1007–1019.
4. Tan H and Pillai KM. Multiscale modeling of unsaturated flow in dual-scale fiber preforms of liquid composite molding I: Isothermal flows. *Compos A Appl Sci Manuf* 2012; 43: 1–13.

5. Dimitrovova Z and Advani SG. Mesolevel analysis of the transition region formation and evolution during the liquid composite molding process. *Comput Struct* 2004; 82: 1333–1347.
6. Schell JSU, Deleglise M, Binetruy C, et al. Numerical prediction and experimental characterisation of meso-scale-voids in liquid composite moulding. *Compos A Appl Sci Manuf* 2007; 38: 2460–2470.
7. Jinlian H, Yi L and Xueming S. Study on void formation in multi-layer woven fabrics. *Compos A Appl Sci Manuf* 2004; 35: 595–603.
8. Varna J, Joffe R, Berglund LA, et al. Effect of voids on failure mechanisms in RTM laminates. *Compos Sci Technol* 1995; 53: 241–249.
9. Leclerc JS and Ruiz E. Porosity reduction using optimized flow velocity in Resin Transfer Molding. *Compos A Appl Sci Manuf* 2008; 39: 1859–68.
10. Lee DH, Lee W II and Kang MK. Analysis and minimization of void formation during resin transfer molding process. *Compos Sci Technol* 2006; 66: 3281–3289.
11. Kang MK, Lee W II and Hahn HT. Formation of microvoids during resin-transfer molding process. *Compos Sci Technol* 2000; 60: 2427–2434.
12. Park CH, Lebel A, Saouab A, et al. Modeling and simulation of voids and saturation in liquid composite molding processes. *Compos A Appl Sci Manuf* 2011; 42: 658–668.
13. Lawrence JM, Neacsu V and Advani SG. Modeling the impact of capillary pressure and air entrapment on fiber tow saturation during resin infusion in LCM. *Compos A Appl Sci Manuf* 2009; 40: 1053–1064.
14. Matsuzaki R, Kobayashi S, Todoroki A, et al. Flow control by progressive forecasting using numerical simulation during vacuum-assisted resin transfer molding. *Compos A Appl Sci Manuf* 2013; 45: 79–87.
15. Foley ME. Modeling the effect of fiber diameter and fiber bundle count on tow impregnation during liquid molding processes. *J Compos Mater* 2005; 39: 1045–1065.
16. Okabe T, Matsutani H, Honda T, et al. Numerical simulation of microscopic flow in a fiber bundle using the moving particle semi-implicit method. *Compos A Appl Sci Manuf* 2012; 43: 1765–1774.
17. Devalve C and Pitchumani R. Simulation of void formation in liquid composite molding processes. *Compos A Appl Sci Manuf* 2013; 51: 22–32.
18. Yashiro S, Nakashima D, Oya Y, et al. Particle simulation of dual-scale flow in resin transfer molding for process analysis. *Compos A Appl Sci Manuf* 2019; 121: 283–288.
19. Garcia JA, Gascon Li, Chinesta F, et al. An efficient solver of the saturation equation in liquid composite molding processes. *Int Mater Form* 2010; 3: S1295–S1302.
20. Matuzaki R, Seto D, Naito M, et al. Analytical prediction of void formation in geometrically anisotropic woven fabrics during resin transfer molding. *Compos Sci Technol* 2015; 107: 154–161.
21. Oyama A, Obayashi S and Nakahashi K. Real-coded adaptive range genetic algorithm applied to transonic wing optimization. *Appl Soft Comput* 2001; 1: 179–187.
22. Ghiasi H, Pasini D and Lessard L. Pareto frontier for simultaneous structural and manufacturing optimization of a composite part. *Struct Multidiscip Optim* 2010; 40: 497–511.
23. Matsuzaki R, Ishikawa T, Okabe T, et al. Stiffness and permeability multi-objective optimization of carbon-fiber-reinforced plastic mesostructures using homogenization method. *J Compos Mater* 2018; 0: 1–16.
24. Kohonen T. The self-organizing map. *Neurocomputing* 1998; 21: 1–6.
25. Okabe T, Oya Y, Yamamoto G, et al. Multi-objective optimization for resin transfer moulding process. *Compos A Appl Sci Manuf* 2016; 92: 1–9.
26. Mathur R, Advani SG and Fink BK. Use of genetic algorithms to optimize gate and vent locations for the resin transfer molding process. *Polym Compos* 1999; 20: 167–178.
27. Kim BY, Nam GJ and Lee JW. Optimization of filling process in RTM using a genetic algorithm and experimental design method. *Polym Compos* 2002; 23: 72–86.
28. Ratle F, Achim V and Trochu F. Evolutionary operators for optimal gate location in liquid composite moulding. *Appl Soft Comput J* 2009; 9: 817–823.
29. Kuentzer N, Simacek P, Advani SG, et al. Permeability characterization of dual scale fibrous porous media. *Compos A Appl Sci Manuf* 2006; 37: 2057–2068.
30. Scholz S, Gillespie JW and Heider D. Measurement of transverse permeability using gaseous and liquid flow. *Compos A Appl Sci Manuf* 2007; 38: 2034–2040.
31. Wu X, Li J and Shenoi RA. A new method to determine fiber transverse permeability. *J Compos Mater* 2007; 41: 747–756.
32. Weitzenböck J, Shenoi R and Wilson P. Radial flow permeability measurement. Part A: Theory. *Compos A Appl Sci Manuf* 1999; 30: 781–796.
33. Plank B, Mayr G, Reh G, et al. Evaluation and visualization of shape factors in dependence of the void content within CFRP by means of X-ray computed tomography. In: *11th European conference on non-destructive testing*, 6–10 October 2014, Prague, Czech Republic.
34. Olivier P, Cottu JP and Ferret B. Effects of cure cycle pressure and voids on some mechanical properties of carbon/epoxy laminates. *Composites* 1995; 26: 509–515.
35. Mehdikhani M, Gorbatikh L, Verpoest I, et al. Voids in fiber-reinforced polymer composites: a review on their formation, characteristics, and effects on mechanical performance. *J Comp Mat* 2019; 53: 1579–1669.